Raman Spectroscopy

Deutsche Ausgabe: DOI: 10.1002/ange.201508218
Internationale Ausgabe: DOI: 10.1002/anie.201508218

Visualization of Vibrational Modes in Real Space by Tip-Enhanced Non-Resonant Raman Spectroscopy

*Sai Duan, Guangjun Tian, and Yi Luo**

Abstract: *We present a general theory to model the spatially resolved non-resonant Raman images of molecules. It is predicted that the vibrational motions of different Raman modes can be fully visualized in real space by tip-enhanced non-resonant Raman scattering. As an example, the non-resonant Raman images of water clusters were simulated by combining the new theory and first-principles calculations. Each individual normal mode gives rise its own distinct Raman image, which resembles the expected vibrational motions of the atoms very well. The characteristics of intermolecular vibrations in supermolecules could also be identified. The effects of the spatial distribution of the plasmon as well as nonlinear scattering processes were also addressed. Our study not only suggests a feasible approach to spatially visualize vibrational modes, but also provides new insights in the field of nonlinear plasmonic spectroscopy.*

Vibrations are intrinsic features of molecules that provide information on how each atom in the molecule moves in space. Vibrational motion can theoretically be well described by quantum mechanics; however, it has never been visualized experimentally in real space simply owing to a lack of suitable experimental methods. The basic requirement for visualizing vibrations is to achieve sufficient spatial and energy resolution. In this context, tip-enhanced Raman scattering (TERS)[1–4] is particularly relevant and promising owing to its exceptional spatial resolution resulting from the spatially confined plasmon (SCP).[5–11] Recently, the resolution of TERS has reached sub-nanometer level under resonant Raman conditions, which opens the door to optically image the inner structure and configuration of a single molecule.[12] It was shown in our recent study[13] that under such conditions, the spatial distribution of the plasmonic field becomes comparable to the size of the molecule, and the interaction between field and matter can no longer be described by conventional response theory. A new theory that considers the effects of the highly confined plasmonic field on the optical transition matrix of the molecule was developed and successfully applied to model the resonant Raman images.[13] We have also found that the resonant Raman image mainly reflects the electronic transition density of the molecule, which is dominated by Franck–Condon contributions that are in turn insensitive to the vibrational modes.[13] Vibrationally resolved Raman images of a molecule can be obtained when Herzberg–Teller contributions are strongly enhanced, which can in principle be achieved in non-resonant Raman processes.

Herein, we have extended our theory recently developed for resonant Raman scattering in the confined plasmonic field to non-resonant cases. We have chosen an important hydrogen-bonding system, namely water clusters, to demonstrate the applicability of the new theory and to make important predictions. At this stage, the sum-over-state expressions with the inclusion of the localized field were derived with the help of our recently established state-to-state mapping between Albrecht's theory and perturbation theory[14] (see the Supporting Information) to model the non-resonant Raman images. More specifically, the amplitude of the linearly induced dipole moment that can be computed by first-principles methods is given as

$$\mu^{L}_{k,\mathrm{ind}} = \sqrt{F_P} M_i E^0_i \frac{\partial \alpha_{\mathrm{eff}}}{\partial Q_k} \langle v^f | Q_k | v^i \rangle \tag{1}$$

with a matrix element of

$$\alpha_{\mathrm{eff},pq} = 2 \sum_r \frac{\langle \psi_g | \hat{p} | \psi_r \rangle \langle \psi_r | \hat{q} g | \psi_g \rangle}{\Delta E_{rg}} \tag{2}$$

where p and q are the Cartesian coordinates. Here, the frequency of the incident light could be assumed to be zero owing to the non-resonant conditions, F_P is the Purcell factor, which is independent of the position of the TERS tip in the xy plane and molecular vibrations, E^0_i is the electric field amplitude of the incident laser, M_i is the enhancement factor of the SCP with respect to the incident laser, Q_k is the corresponding normal mode, $|v^i\rangle$ and $|v^f\rangle$ are the initial and final vibrational states in the electronic ground state $|\psi_g\rangle$, $|\psi_r\rangle$ is the excited electronic state, g is the corresponding distribution function of the electric field amplitude of the SCP, which is obviously related to the tip position, and ΔE_{rg} is the vertical excitation energy. According to previous studies, the zero-frequency limit used here is a good approximation for water molecules because of the large energy gap between the ground and excited states.[15]

[*] Dr. S. Duan, Dr. G. Tian, Prof. Dr. Y. Luo
Department of Theoretical Chemistry and Biology
School of Biotechnology, Royal Institute of Technology
10691 Stockholm (Sweden)
Prof. Dr. Y. Luo
Hefei National Laboratory for Physical Sciences at the Microscale and Synergetic Innovation Center of Quantum Information & Quantum Physics
University of Science and Technology of China
Hefei, 230026 Anhui (P. R. China)
E-mail: yiluo@ustc.edu.cn

Supporting information and ORCID(s) from the author(s) for this article are available on the WWW under http://dx.doi.org/10.1002/anie.201508218.

Remarkably, the derivative of α_{eff}, which includes g, with respect to Q_k in Eq. (1) reveals that Raman images are related to individual vibrational modes. In other words, we expected that vibrational modes could be visualized through non-resonant Raman images. We would like to emphasize again that in conventional response theory, the transition integrals are calculated from $\langle \psi_g | \hat{\mathbf{r}} | \psi_r \rangle$ ($\hat{\mathbf{r}}$ is the electron position operator),[16–23] which is not related to the position of the TERS tip. Therefore, the theory of uniform interactions between the SCP and adsorbates is invalid for high-resolution Raman images. For the sake of simplification, we only evaluated the zz component of Eq. (2) and chose s-type Gaussian functions for g. Once the amplitude of the induced dipole had been obtained, the corresponding Raman intensity could be readily calculated:[17]

$$I_k^L = \frac{\pi^2 c \tilde{\nu}_s^4 M_d^2 \left|\mu_{k,\text{ind}}^L\right|^2}{2\varepsilon_0} \tag{3}$$

where c is the speed of light, $\tilde{\nu}_s$ is the wavenumber of scattering, ε_0 is the permittivity of free space, and M_d is the directional radiation pattern factor.[23] The experimental setup for TERS is shown in the Supporting Information, Figure S1. We will focus on the contrast or the relative Raman intensity from different grid points, which were also experimentally determined.[12] Apparently, to fully distinguish different vibrational modes in real space, an SCP that is as small as possible needs to be achieved. We noticed that the highest confinement for SCP had previously been estimated to be 1 Å.[24] For the sake of clarity, we have set the full width at half maximum (FWHM) for the x and y components of g to its theoretical limit, 1 Å (for theoretical background and computational details, see the Supporting Information).[24]

We started our analysis with calculations for a water monomer on a Au(111) surface. The choice of a Au(111) surface was motivated by its inertness with respect to water[25,26] as well as its beneficial properties for the generation of SCP.[27,28] Owing to the limitations of the computational methods employed, we only calculated the excited states of the adsorbates, neglecting the effects of the weak interaction between adsorbate and substrate.

The optimized geometry of a water monomer adsorbed on a Au(111) surface is depicted in Figure 1 A. It clearly shows that the water adsorbed 2.7 Å above the top site and has a tilted configuration with an angle of 7°, consistent with previous theoretical results.[29,30] Simulated non-resonant Raman images of all vibrations of the water monomer are given in Figure 1 B. We immediately noticed that the non-resonant Raman images are indeed vibration-dependent. Specifically, the image of the bending mode (ν_2) shows a strong, bell-shaped, bright spot associated with the oxygen atom and a moderately bright ribbon between the two hydrogen atoms. For the symmetric (ν_1) and antisymmetric (ν_3) stretching modes, the images show similar patterns for the hydrogen atoms. On the other hand, some differences associated with the oxygen atom can be seen in Figure 1 B. For ν_1, the oxygen and hydrogen atoms are connected, whereas for ν_3, there are two weak lobes between them. The slight symmetry breaking should be attributed to the interactions between the adsorbates and the substrate as the result of geometry optimization. It should be noted that a slight change in the height of the scanning plane and the inclusion of the frequency of the incident light do not alter the images (Figure S2).

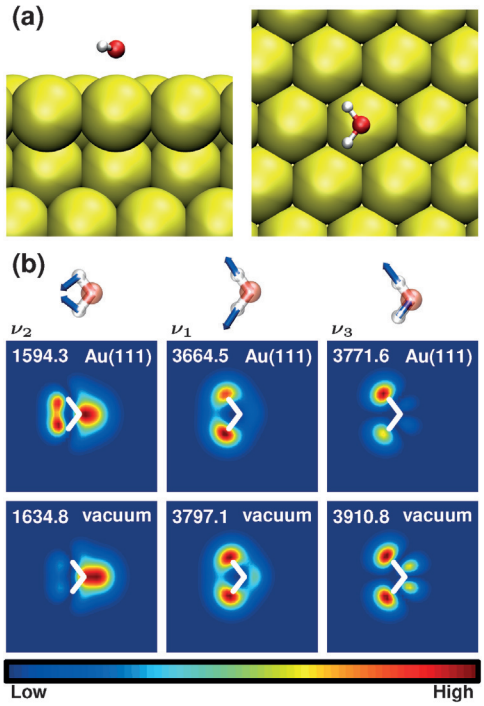

Figure 1. a) Top view (left) and side view (right) of the optimized geometry for a water monomer adsorbed on a Au(111) surface. b) Simulated non-resonant Raman images for the vibrational modes of a water molecule adsorbed on a Au(111) surface (top) and in vacuum (bottom). The values are the corresponding frequencies in cm^{-1}.

For comparison, Figure 1 B also shows calculated images for a free water molecule in the xy plane. As expected, the structures are symmetric and generally resemble their counterparts on the Au(111) surface very well. The most noticeable difference is the contrasts, that is, the oxygen patterns are more pronounced in the images of free water molecules (see Figure 1 B). This difference should be attributed to the tilted configuration of the adsorption, where the oxygen atom is farther away from the plasmonic center. It is noteworthy that the phase of the pattern represents the sign of $\partial\alpha_{\text{eff}}/\partial Q_k$. For instance, the ribbon- and the bell-shaped patterns in the ν_2 image have different phases whereas all patterns in the ν_1 image have the same phase. Furthermore, the phases of the four patterns in the ν_3 image (two strong and two weak lobes) are the same as that of the d_{xy} atomic orbital (Figure S3).

We then moved on to consider a water dimer, which is the simplest water cluster. The optimized geometry of a water dimer adsorbed on a Au(111) surface (Figure 2 A) shows that the two water molecules are both adsorbed on top sites. One water molecule (labeled as W_O) has a similar configuration to that of the monomer. However, owing to the influence of the other water molecule, W_O is 0.2 Å closer to the substrate, and the tilt angles (16° and 18° for the two OH bonds) are greater than those of the monomer. Meanwhile, the other water

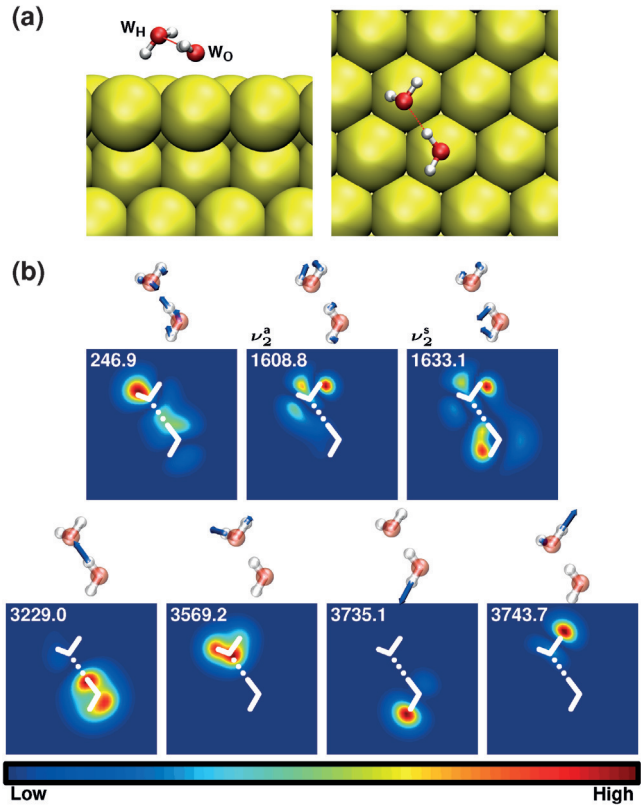

Figure 2. a) Top view (left) and side view (right) of the optimized geometry for a water dimer adsorbed on a Au(111) surface. b) Simulated non-resonant Raman images for a water dimer showing hydrogen-bond stretching, bending, and stretching modes. The values are the corresponding frequencies in cm^{-1}.

molecule (W_H) has one hydrogen atom pointing to the substrate. In W_H, the oxygen atom is 0.7 Å farther away from the substrate than that in W_O. This configuration is consistent with water dimers adsorbed on other metal surfaces.[31,32] A helicopter-like rotation of the water dimer adsorbed on the Pt(111) surface around W_O was identified by scanning tunneling microscopy.[33] However, for simplicity, we neglect this rotation in the simulation of Raman images. We should emphasize that the rotation may be hindered on other inert surfaces.[34]

The images calculated for the water dimer are shown in Figure 2B. The image of the vibration related to the hydrogen bond is characterized by stretching between W_O and W_H. Calculations show that this mode is the only band in the range of 200 to 300 cm^{-1}, which highlights the advantage of the spectral window for Raman images. We observed a moderately bright area between W_O and W_H for this mode in Figure 2B, indicating that Raman spectroscopy can be used to detect vibrations related to hydrogen bonds. In the bending region around 1600 cm^{-1}, there are two bands that are due to the antisymmetric (with low frequency, labeled as ν_2^a) and symmetric (with high frequency, labeled as ν_2^s) mixing of ν_2 modes. In their mixing, ν_2^a has more proportion of W_H, while ν_2^s has more proportion of W_O. In the ν_2^s image, the pattern for W_O contains a bright ribbon, which is consistent with that of the ν_2 mode of the monomer. Meanwhile, the image associated with the oxygen atom in W_O is obscure because of the large tilted angle. The patterns for W_H in the ν_2^a and ν_2^s images are similar, and both are significantly different from that in the monomer. This could be attributed to the fact that the configuration of W_H is obviously different from that of the monomer (see Figure 1A and Figure 2A). Moreover, the highlighted pattern of W_H for ν_2^s could be attributed to the fact that the position of W_H is closer to the plasmonic center. All of these results demonstrate that Raman images can provide detailed information on molecular configuration. In the stretching region (Raman shift >3000 cm^{-1}), however, the vibrational modes are more localized with less mixing. In spite of this, the ν_1 and ν_3 modes can still be distinguished from the Raman images. The two ν_1 images are associated with the whole corresponding water molecules, whereas the images of ν_3 are more concentrated on the hydrogen atoms.

We then turned our attention to a more complicated water cluster, namely a water trimer. The optimized geometry shown in Figure 3A shows several distinct features. First, all water molecules possess a configuration similar to that of the monomer and are located around 2.9 Å above the substrate. The tilt angles are 5° and 15° for the hydrogen-bonded OH in the ring and the free OH group, respectively. Moreover, the whole system has approximate C_3 symmetry (Figure 3A).This configuration is consistent with previous results for a water trimer adsorbed on a Pt(111) surface.[31] For convenience, hereafter, we refer to the bottom, right, and left water molecules as W_B, W_R, and W_L, respectively.

In the hydrogen-bond stretching region, there are three vibrational modes for the water trimer. Within the approximated C_3 symmetry, the two modes with lower frequency belong to the degenerate asymmetric stretching of the hydrogen bonds.[35] The mode located at 231.8 cm^{-1} mainly results from stretching of the hydrogen bond between W_R and W_L. Thus, the image is similar to its dimer counterpart where a moderately bright area was observed between W_R and W_L. The vibration located at 238.7 cm^{-1} is the other degenerate mode that is mainly due to stretching of the hydrogen bonds between W_B and W_L as well as W_B and W_R. As a result, the hydrogen bonds between them have been highlighted in the Raman image. The symmetric stretching mode (ring breathing mode) is located at 289.5 cm^{-1}. The constructive coherence of the hydrogen bonds leads to the brighter center of the trimer ring. In this case as well as in those to follow, the symmetry breaking observed in the Raman images should again be attributed to interactions between the adsorbates and the substrate.

The symmetry assignments in the bending region are the same as those in the hydrogen-bond stretching region. We could clearly observe the ν_2 image pattern of the monomer for the degenerate asymmetric modes. The constructive coherence between the ribbon- and bell-shaped patterns for different water molecules is noticeable in the images, which could be attributed to the phases in the ν_2 image of the monomer. For the same reason, for the symmetric mode in the same region, destructive coherence between all water molecules leads to the bright ribbon pattern and the obscure bell-shaped pattern shown in Figure 3B.

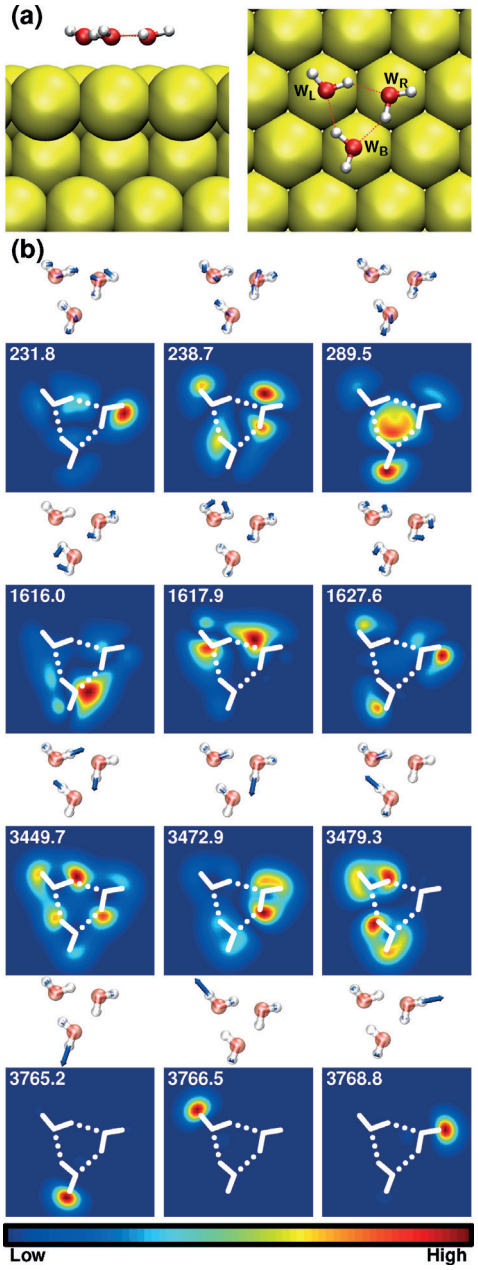

Figure 3. a) Top view (left) and side view (right) of the optimized geometry of a water trimer adsorbed on a Au(111) surface. b) Simulated non-resonant Raman images for a water trimer showing hydrogen-bond stretching, bending, and stretching modes. The values are the corresponding frequencies in cm^{-1}.

In contrast, the symmetric assignments in the stretching region are different. For ν_1, the mode with the lowest frequency belongs to the symmetric mode. Here, we could observe constructive coherence between the water molecules. The other two modes could be categorized as degenerate modes. The simulations show that the Raman image concentrates on W_R for the lower band and on both W_L and W_B for the higher one. For ν_2, the vibrational modes are highly localized, and the symmetry assignment of them is indistinct. In these cases, the simulated Raman images only associate with the hydrogen that has the major component of the normal modes.

From an experimental perspective, it is more feasible to work with a larger SCP. However, a larger size could lead to lower spatial resolution. Our calculations have shown (Figure S4–S6) that with a larger SCP, the Raman images become defocused and provide less information on molecular details. For instance, the moderately bright area between the different water molecules for hydrogen-bonding vibrations of the water trimer (238.1 and 238.7 cm^{-1}) is absent when the size of the SCP is set to 5 Å (see Figure 4, top). In general, improved

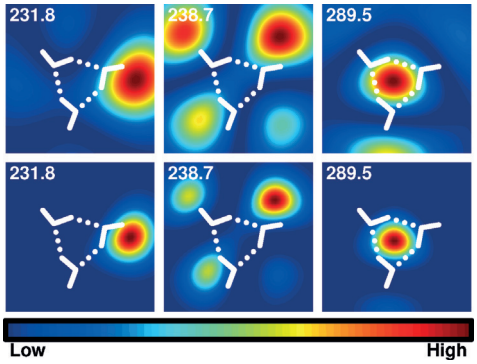

Figure 4. Simulated linear (top) and nonlinear (bottom) non-resonant Raman images for the hydrogen-bond stretching modes of a water trimer adsorbed on a Au(111) surface when the *x* and *y* components of FWHM are set to 5 Å. The values are the corresponding frequencies in cm^{-1}.

results may be anticipated with the inclusion of nonlinear processes.[19,36] In this case, the amplitude of the nonlinearly induced dipole could be estimated as (see the Supporting Information for details):

$$\mu^{NL}_{k,\mathrm{ind}} = \lambda \frac{\partial \alpha_{\mathrm{eff}}}{\partial Q_k} \frac{\partial \alpha'_{\mathrm{eff}}}{\partial Q_k} \langle v^f | Q_k | v^i \rangle^2 \tag{4}$$

where λ [Eq. (S13)] is a constant independent of the tip position and

$$\alpha'_{\mathrm{eff},pq} = 2 \sum_{r'} \frac{\langle \psi_g | \hat{p} g | \psi_{r'} \rangle \langle \psi_{r'} | \hat{q} g | \psi_g \rangle}{\Delta E_{r'g}} \tag{5}$$

By comparing the linear (top) and nonlinear (bottom) results shown in Figure 4, we found that nonlinear processes can indeed improve image resolution. However, with a larger SCP, the molecular details are still largely missing even when nonlinear processes are included (see Figure S7–S10 for more results).

In summary, we have developed a theoretical framework for modeling non-resonant Raman images of molecules under a highly confined plasmonic field. By using first-principles calculations, vibrationally resolved Raman images of the water clusters were predicted, which strongly suggest that tip-enhanced non-resonant Raman scattering is capable of visualizing the vibrational motion of molecules in real space, and even the effects of hydrogen bonds on the vibrations. Our proposed computational approach could be significantly improved by employing the coupled-perturbed

method,[37] so that much larger and more complicated molecular or biological systems can be explored in the future.

Acknowledgements

This work was supported by the Strategic Priority Research Program of the Chinese Academy of Sciences (XDB01020200), the Göran Gustafsson Foundation for Research in Natural Sciences and Medicine, and the Swedish Research Council (VR). The Swedish National Infrastructure for Computing (SNIC) is acknowledged for providing computer time.

Keywords: ab initio calculations · Raman spectroscopy · surface chemistry · vibrational spectroscopy · water adsorption

How to cite: *Angew. Chem. Int. Ed.* **2016**, *55*, 1041 – 1045
Angew. Chem. **2016**, *128*, 1053 – 1057

[1] R. M. Stöckle, Y. D. Suh, V. Deckert, R. Zenobi, *Chem. Phys. Lett.* **2000**, *318*, 131 – 136.
[2] M. S. Anderson, *Appl. Phys. Lett.* **2000**, *76*, 3130 – 3132.
[3] N. Hayazawa, Y. Inouye, Z. Sekkat, S. Kawata, *Opt. Commun.* **2000**, *183*, 333 – 336.
[4] B. Pettinger, G. Pucardi, R. Schuster, G. Ertl, *Electrochem. Jpn.* **2000**, *68*, 942 – 949.
[5] A. Hartschuh, E. J. Sánchez, X. S. Xie, L. Novotny, *Phys. Rev. Lett.* **2003**, *90*, 095503.
[6] N. Anderson, A. Hartschuh, S. Cronin, L. Novotny, *J. Am. Chem. Soc.* **2005**, *127*, 2533 – 2537.
[7] J. Steidtner, B. Pettinger, *Phys. Rev. Lett.* **2008**, *100*, 236101.
[8] T. Ichimura, S. Fujii, P. Verma, T. Yano, Y. Inouye, S. Kawata, *Phys. Rev. Lett.* **2009**, *102*, 186101.
[9] T. Yano, P. Verma, Y. Saito, T. Ichimura, S. Kawata, *Nat. Photonics* **2009**, *3*, 473 – 477.
[10] J. Stadler, T. Schmid, R. Zenobi, *Nano Lett.* **2010**, *10*, 4514 – 4520.
[11] C. Chen, N. Hayazawa, S. Kawata, *Nat. Commun.* **2014**, *5*, 3312.
[12] R. Zhang, Y. Zhang, Z. C. Dong, S. Jiang, C. Zhang, L. G. Chen, L. Zhang, Y. Liao, J. Aizpurua, Y. Luo, J. L. Yang, J. G. Hou, *Nature* **2013**, *498*, 82 – 86.
[13] S. Duan, G. Tian, Y. Ji, J. Shao, Z. C. Dong, Y. Luo, *J. Am. Chem. Soc.* **2015**, *137*, 9515 – 9518.
[14] Z.-Y. Gong, G. Tian, S. Duan, Y. Luo, *J. Chem. Theory Comput.* **2015**, *11*, 5385 – 5390.
[15] C. Van Caillie, R. D. Amos, *Phys. Chem. Chem. Phys.* **2000**, *2*, 2123 – 2129.
[16] A. C. Albrecht, *J. Chem. Phys.* **1961**, *34*, 1476 – 1484.
[17] J. Neugebauer, M. Reiher, C. Kind, B. A. Hess, *J. Comput. Chem.* **2002**, *23*, 895 – 910.
[18] D. J. Masiello, G. C. Schatz, *Phys. Rev. A* **2008**, *78*, 042505.
[19] S.-Y. Lee, D. Zhang, D. W. McCamant, P. Kukura, R. A. Mathies, *J. Chem. Phys.* **2004**, *121*, 3632 – 3642.
[20] J. J. Sakurai, *Advanced Quantum Mechanics*, Addison-Wesley Pub. Co, Reading, MA, **1967**.
[21] M. O. Scully, M. S. Zubairy, *Quantum Optics*, Cambridge University Press, Cambridge, New York, **1997**.
[22] D. A. Long, *The Raman Effect: A Unified Treatment of the Theory of Raman Scattering by Molecules*, Wiley, Chichester, **2002**.
[23] E. Le Ru, P. Etchegoin, *Principles of Surface-Enhanced Raman Spectroscopy and Related Plasmonic Effects*, Elsevier, Amsterdam, **2009**.
[24] J. M. Atkin, M. B. Raschke, *Nature* **2013**, *498*, 44 – 45.
[25] G.-C. Wang, S.-X. Tao, X.-H. Bu, *J. Catal.* **2006**, *244*, 10 – 16.
[26] A. A. Phatak, W. N. Delgass, F. H. Ribeiro, W. F. Schneider, *J. Phys. Chem. C* **2009**, *113*, 7269 – 7276.
[27] Z. Yang, Q. Li, F. Ruan, Z. Li, B. Ren, H. Xu, Z. Tian, *Chin. Sci. Bull.* **2010**, *55*, 2635 – 2642.
[28] N. Kazemi-Zanjani, S. Vedraine, F. Lagugne-Labarthet, *Opt. Express* **2013**, *21*, 25271 – 25276.
[29] A. Michaelides, V. A. Ranea, P. L. de Andres, D. A. King, *Phys. Rev. Lett.* **2003**, *90*, 216102.
[30] R. Nadler, J. F. Sanz, *J. Chem. Phys.* **2012**, *137*, 114709.
[31] S. Meng, E. G. Wang, S. Gao, *Phys. Rev. B* **2004**, *69*, 195404.
[32] A. Michaelides, K. Morgenstern, *Nat. Mater.* **2007**, *6*, 597 – 601.
[33] K. Motobayashi, C. Matsumoto, Y. Kim, M. Kawai, *Surf. Sci.* **2008**, *602*, 3136 – 3139.
[34] J. Guo, X. Meng, J. Chen, J. Peng, J. Sheng, X.-Z. Li, L. Xu, J.-R. Shi, E. Wang, Y. Jiang, *Nat. Mater.* **2014**, *13*, 184 – 189.
[35] F. Cotton, *Chemical Applications of Group Theory*, Wiley, New York, **1990**.
[36] Y. R. Shen, *The Principles of Nonlinear Optics*, Wiley-Interscience, Hoboken, **2002**.
[37] Y. Osamura, Y. Yamaguchi, H. F. Schaefer III, *Chem. Phys.* **1986**, *103*, 227 – 242.

Received: September 2, 2015
Revised: October 12, 2015
Published online: November 13, 2015

